Pp IX Silica Nanoparticles Demonstrate Differential Interactions with *In Vitro* Tumor Cell Lines and *In Vivo* Mouse Models of Human Cancers

Virginie Simon[1], Corinne Devaux[1], Audrey Darmon[1], Thibault Donnet[1], Edouard Thiénot[1], Matthieu Germain[1], Jérôme Honnorat[2], Alex Duval[3], Agnès Pottier[1], Elsa Borghi[1], Laurent Levy[1] and Julie Marill*[1]

[1]Nanobiotix SA, rue de Wattignies, Paris, France
[2]UMR Inserm-UCBL2 U842, Faculté Laennec, rue G. Paradin, Lyon, France
[3]UMR S893, rue du faubourg Saint Antoine, Paris, France

ABSTRACT

Protoporphyrin IX (Pp IX) silica nanoparticles, developed for effective use in photodynamic therapy (PDT), were explored in *in vitro* and *in vivo* models with the ambition to improve knowledge on the role of biological factors in the photodamage. Pp IX silica nanoparticles are found efficient at temperature with extreme metabolic downregulation, which suggest a high proportion of passive internalization. For the first time, clearance of silica nanoparticles on tumor cells is established. Cell viability assessment in six tumor cell lines is reported. In all tumor types, Pp IX silica nanoparticles are more efficient than free Pp IX. A strong fluorescence signal of reactive oxygen species generation colocalized with Pp IX silica nanoparticles, correlates with 100% of cell death. *In vivo* studies performed in HCT 116, A549 and glioblastoma multiforme tumors-bearing mice show tumor uptake of Pp IX silica nanoparticles with better tumor accumulation than the control alone, highlighting a high selectivity for tumor tissues. As observed in *in vitro* tests, tumor cell type is likely a major determinant but tumor microenvironment could more influence this differential time accumulation dynamic. The present results strongly suggest that Pp IX silica nanoparticles may be involved in new alternative local applications of PDT.

INTRODUCTION

Failure of cancer treatments has been principally attributed to inherent genetic and molecular characteristics of any particular tumor type. Nevertheless, the tumor microenvironment also mediates resistance of solid tumors to cytotoxics and radiation. Solid tumors are composed by two compartments, stroma and malignant cells. Stroma characteristics are heterogeneous across different tumor areas, have intertumor differences for key parameters such as vessels, cytokines, extracellular matrix and fibroblast. Also the tumor size and the host organ may determine the specific microenvironment and influence cell physiology, cell membrane permeability and transport with subsequent proteomic changes.

Regarding the anticancer agents, the understanding of chemistry and its relationship with biological systems, mainly with the *in vivo* complexity, has been subject to extensive research because thought as crucial parameters to determine pharmacokinetic, pharmacodynamic and metabolism.

Meanwhile, the cancer population is changing. About 50% of cancer diagnoses are currently established in patients aged 70 years or older. This proportion will increase as more elderly people survive other disorders, are diagnosed with cancer, and wish to have their disease managed actively.

Therefore, specific management of elderly patients with cancer has become a need. Furthermore, improvement of anticancer approaches has allowed many individuals to achieve long survival. Because of their accrued fragility due to previous therapies, it is essential to offer anticancer approaches based on innovative mechanisms and focused on highly localized efficacy. Oncologists and geriatricians should be provided with opportunities for development of therapy tools that are acceptable to both groups and benefit these patient populations.

Such contributor may be represented by the photodynamic therapy (PDT), which improvement might even challenge pre-irradiated lesions without adding major secondary effects in the surrounding healthy tissues.

Current clinical PDT limitations have also been imputed to constraints related with chemistry, excitation with short wavelength light (630 nm), useful only for treatment of superficial lesions, and too poor tissue selectivity. Indeed, a nontissue specific accumulation has been observed in patients treated with protoporphyrin molecules (1).

In addition, the short migration distance of singlet oxygen would imply strong relationship between subcellular localization of the photosensitizers and the organelles in the close neighborhoods to achieve efficient cell damage (2). In the recent years, this therapy has been successfully used in the management of patients with various malignant tumors, including cancers of the skin (3), gastrointestinal tract (4), lung (5) and uterus (6). Nevertheless, because of the long-lasting skin phototoxicity and applicability on superficial lesions, PDT has only moderately impacted the cancer disease management.

To improve the efficiency of PDT, strategies include chemical changes to achieve wavelength enlargement and formulation innovations to modify features such as cell uptake rate and less classical, intracellular localization. Both ultimately will allow tissue accumulation of the compound with increased selectivity for the type of cell death.

---

*Corresponding author email: julie.marill@nanobiotix.com (Julie Marill)

In essence, a dynamic picture of research on PDT in cancer has grown quickly over the years since its first applications in the clinic. We are closer to an understanding of its multiple factor roles and potential as therapeutic agents. Interpretations to date suggest that the chemistry and delivery systems could be acting at the "cutting edge" of the multifarious environmental signals governing the behavior of tumors and it is instructive to consider them as key factor.

It is interesting to underline that each photosensitizer is given at a fixed dose, defined by systemic dose limiting toxicities as done for other pharmaceuticals intended for systemic use. However, PDT is a paradigm of local treatment. One solution for this paradoxical situation may be to use photosensitizers entrapped in nanosystems. Two different strategies using nanoparticles could be applied: either biodegradable nanoparticles, from which the photosensitizers can be released or, alternatively, nonbiodegradable nanoparticles, for which no release of the photosentitizer is present but instead, it is essential that the oxygen diffuses in and out of the nanoparticles freely.

In the current paper, we present the results regarding different aspects of protoporphyrin IX (Pp IX) silica nanoparticles, an energy-activated nanoparticle product selected from our nanomedicine platform, studied in *in vitro* and *in vivo* models. The potential therapeutic use of silica nanoparticles should take into account the variable aggressiveness of cancer types and growth site of the tumor.

Because resistance to cytotoxics has been found to be related to tumor stroma and microenvironment, which will determine features at the cell level, Pp IX silica nanoparticles were tested on various tumor cell lines, adherent and in suspension. Thus, specificities owed to cell physiology and social life could be captured. Then, three tumor models were used *in vivo* to study the biodistribution of nanoparticles, two human epithelial cancers and one human glioblastoma multiforme. In this way, cell type, engraftment site and stroma contribution were radically different.

Interactions of Pp IX silica nanoparticles with these different biosystems were evaluated focused on human cancer cells and having as ambition to understand better the role of biological factors in the photodamage.

MATERIALS AND METHODS

Human cell lines and tumor models. Six human tumor cell lines were investigated *in vitro*: HCT 116 and HT-29 (colon cancer cell lines), MCF7 and MDA-MB-231 (breast cancer cell lines), A431 (epidermoid cell line) and LLBC37 (lymphoblastoid cell line).

In vivo investigations were performed in tumor-bearing mice, HCT 116 and A549 (lung cancer) models and in a mouse model established from a human glioblastoma multiforme. It had been obtained from a Caucasian male patient and developed by the Neurology Department of the Medical School (Vandoeuvre-lès-Nancy, France) (7).

HT-29, HCT 116, A431, MDA-MB-231 and MCF7 were obtained from the American Type Culture Collection (LGC Promochem, Molsheim, France). HCT 116 and HT-29 cells were maintained in McCoy's 5a medium; A431, LLBC37, MCF7 and A549 in Dulbecco's modified Eagle's medium; and MDA-MB-231 in Leibovitz's L-15 Medium with GlutaMAX™. All cell lines were supplemented with 10% (vol/vol) heat-inactivated fetal calf serum (FCS) and kept in 5% CO_2 at 37°C except for MDA-MB-231 kept at 0% CO_2.

Buffers and reagents. All reagents were obtained from commercial sources, the WST-1 reagent for the determination of cell viability from Roche (Basel, Switzerland). Slow fade reagent with diaminophenylindol (DAPI) and 3′-(*p*-aminophenyl) fluorescein (APF) kits were purchased from Molecular Probes (Cergy Pontoise, France). Cell culture reagents were supplied by Invitrogen (Cergy Pontoise, France).

Tested products. Protoporphyrin IX (excitation: 630 nm; emission: 630–704 nm; absorption: 408 nm) was purchased from Sigma-Aldrich (Saint Quentin Fallavier, France). Pp IX silica nanoparticles are composed of Pp IX core encapsulated in a silica shell. Three different Pp IX nanoparticles sizes were obtained by modifying the synthesis process mainly in terms of temperature: 10, 25 and 60 nm. Nanoparticles sizes were evaluated by transmission electron microscopy (TEM), JEOL 100C× electron microscope, operating at an accelerated voltage of 100 kV; lens 23 000×. The Pp IX nanoparticles were synthesized in controllable chemical reactor in Nanobiotix SA (Paris, France).

In a typical experiment, the micelles were prepared by dissolving Tween 80 (5.5 g) and 1-butanol (6 mL) in ultra pure water (200 mL) under vigorous magnetic stirring. Ammonia (10 м, 200 μL) was added. The resulting clear solution was then transferred to a reactor (250 mL double layer glass reactor from Bercauverre-France, equipped with a stirrer dissolving from Fisher). The solution was allowed to stabilize at a temperature of 27 ± 0.5°C under stirring. Pp IX in DMF (71.6 mм, 1.5 mL) was dissolved in solution. Neat triethoxyvinylsilane (2 mL) was added to the micellar system, and the resulting solution was stirred for about 24 h. At the end of the process, surfactant Tween 80 and cosurfactant 1-butanol were removed by dialyzing the solution against cold water (4°C) in a 12–14 kDa cutoff cellulose membrane (Cellusep T3-45-15, from Interchim). The dialysis water was changed once a day for 120 h. The dialyzed solution was then concentrated by a factor about 10 using an ultrafiltration device (Amicon stirred cell model 8400 from Millipore) with a 30 kDa cellulose membrane. The resulting solution was ultimately filtered through a 0.22 μm cutoff membrane filter (PES membrane from Millipore) under laminar hood. Sterilized PBS 10× solution (1 mL) was added to the prepared sterilized solution (9 mL) under laminar hood and used for further experimentation.

Protoporphyrin IX silica nanoparticles were stocked at 4°C for several months. Furthermore, composite Pp IX nanoparticles containing dioctadecyl tetramethyl indodicarbocyanine chloro benzene (DID) tracer (Molecular Probes) were prepared in a similar way as above described to visualize their biodistribution in mouse models after intravenous injection of the product. These nanoparticles are composed of silica shell that contained Pp IX with DID tracer entrapped in the silica matrix. Proportion of dyes within any silica nanoparticle was Pp IX 97% and 3% of DID tracer. DID (excitation: 644 nm and emission: 665 nm) is formulated in dimethyl sulfoxide and is useful for avoidance of autofluorescence and phototoxic effects. For all *in vitro* experiments, Pp IX silica nanoparticles were used in medium containing 10% FCS.

Photonics activation. A lamp device was designed in order to improve homogeneity of light dose when exposing 96 well plates containing the tested cells. Briefly, it is composed of 88 diodes, each emitting light at 630 nm, organized on a plate and can illuminate two 96 well plates simultaneously (Intellibio, Nancy, France). The total fluence of lamp is 4 mW cm^{-2}. Controls of nonilluminated 96 well plates were covered with aluminum foil.

Cell uptake of Pp IX silica nanoparticles. Nanoparticles tumor cell uptake experiments were performed on HT-29, HCT 116, A431, LLBC37, MDA-MB-231 and MCF7 cell lines; 2×10^5 cells mL^{-1} (5×10^4 cells per well) were seeded on eight Lab-Tek glass slides (Dutscher, Issy-les-Moulineaux, France) 12–14 h before photosensitizer incubation. Cells were treated with 5 μM of Pp IX silica nanoparticles or with free Pp IX, for 1 h at 37°C. After incubation, cells were washed with PBS 1x, fixed using formalin solution 8% (Sigma-Aldrich) and stained with slow fade antifade reagent with DAPI (Invitrogen). Slides were analyzed observed with D1 Zeiss microscope and photographed with an Axio Cam MRm camera; lens 40× (Zeiss, Le Pecq, France). Images were analyzed using the laser scanning microscopes Image Browser software (Zeiss).

Quantification analysis of the internalized nanoparticles. Assays were performed in six well microplates. HCT 116 and HT-29 cell lines were seeded at the density of 10^6 cells/mL and incubated in the presence of 5 μM of Pp IX silica nanoparticles for 0.5, 1 and 3 h at 37°C or 4°C. After incubation, cells were washed once with PBS 1x. Cells were counted and then lysed in buffer (NaOH 1 м) at 4°C for 30 min.

Homogenates were centrifuged and supernatants were used for Pp IX quantification using UV spectrophotometer (Bio-Rad, Marnes la Coquette, France). Results were compared with a standardized curve obtained for Pp IX silica nanoparticles.

Evaluation of Pp IX silica nanoparticles effect on cell survival. The cell viability assay is based on the cleavage of the tetrazolium salt, WST-1 (4-[3-(4-iodophenyl)-2-(4-nitrophenyl)-2*H*-5-tetrazolio]-1,3-benzene disulfonate), by mitochondrial dehydrogenases in viable cells to form highly water-soluble formazan.

Four experimental groups were tested, Pp IX silica nanoparticles and free Pp IX groups, treated or not with light activation. Assays were performed on HT-29, HCT 116, A431, MDA-MB-231, LLBC37 and MCF7 cell lines in 96 well microplates; 12 000 cells were incubated in the presence of increasing concentrations of Pp IX silica nanoparticles up to 100 μM. After 3 h of incubation, cells were rinsed once with PBS 1x and fresh complete medium was added. Cells were illuminated at time 0, 2, 5 and 24 h after incubation with lamp during 20 min and WST-1 assay was performed after 48 h.

Cells were incubated for 2 h with 10 μL of WST-1 to achieve 1:10 final dilution. The absorbance of the converted dye was measured at a wavelength of 450 nm. Cell viability rate was calculated based on the absorbance measured relative to that of control cultured cells.

Reactive oxygen species (ROS) detection. Assay was performed in 96 well white plates (Nunc, Fischer Scientific, Ilkirch, France). HCT 116 and HT-29 cells (12 000 per well) were incubated in the presence of increasing concentrations of Pp IX silica nanoparticles and free Pp IX up to 100 μM for 3 h at 37°C. After incubation, cells were washed once with PBS 1x; fresh medium was added with 5 μM of APF, ROS detection kit. Then, cells were illuminated with lamp for 20 min. Measures were performed with fluorescence spectrophotometer (Varian, Les Ulis, France), excitation spectrum was 490 nm, emission spectrum was 515 nm and gain 650 V. Results were analyzed using the Cary Elipse software.

Mouse xenografted tumor models. Biodistribution of Pp IX silica nanoparticles loaded with DID tracer was studied in three different *in vivo* tumor models. Female athymic Swiss nude mice (Charles River Laboratories, Arbresle, France) and female athymic Naval Medical Research Institute nude mice (Janvier, le Genest Saint Isle, France), weighing 20–25 g, aged 5–7 weeks, were injected subcutaneously (flank) with two tumor cell lines, HCT 116 (10 millions cells) and A549 (20 millions cells), respectively. Furthermore, a glioblastoma multiforme (10 mm³ fragment) was subcutaneously implanted in the right posterior inguinal pit of male mice (athymic Nude-*Foxn1^{nu}* mice 5 weeks from Harlan Europe) and was also used for evaluation of biodistribution of Pp IX silica nanoparticles loaded with DID tracer (7).

Free DID tracer was also explored in the A549 mouse model to establish prospective comparator for the biodistribution evaluation of nanoparticles loaded with the dyes.

Tumor growth was monitored twice a week. These experiments were performed in conformity with the laws and regulations for experiments with live animals and they were approved by the Animal Board under the Ministry of Agriculture in France.

In vivo optical imaging of tumor-bearing mice. Mice-bearing HCT 116, A549 and glioblastoma multiforme tumors, size 120–500 mm³ were used for imaging experiments. Anesthetized mice (isoflurane/oxygen 3.5% for induction and 1.5% thereafter) received an intravenous injection (tail vein) of 10 mL kg^{-1} of Pp IX silica nanoparticles loaded with DID (2.5 mM Pp IX) tracer in 5% glucose solution. Mice were imaged at different time points postinjection, over 24 h (0, 0.25, 1, 3 ± 3, 15 and 24 h) for the three tumor models.

Fluorescence reflectance imaging was performed using a Hamamatsu optical imaging system described previously (8,9). Briefly, imaging was carried out in a dark box, and anesthetized animals were illuminated with a monochromatic 660 nm light (50 μW cm^{-2}). The re-emitted fluorescence was filtered using a colored glass filter RG 665 (optical density > 5 at the excitation wavelength 633 nm) and collected with a cooled (−70°C) digital charge-coupled device camera (Hamamatsu digital camera). All fluorescence images were acquired using 100 ms of exposure time for glioblastoma multiforme model, 20 ms for HCT 116 and 200 ms for A549 models, respectively. Other related parameters were kept constant throughout the experiment. Images were acquired as 16 bit TIFF files which can provide a dynamic of up to 65 535 gray levels. Image processing used in this study, including setting look-up-table range and measurement of the fluorescence intensity for each region of interest (ROI), were performed using the Wasabi software (Hamamatsu). It is important to note that all images are presented without background subtraction. For quantifying tumor contrast, the mean fluorescence intensities of the tumor area (*T*) and contralateral skin area (*S*) were calculated. Dividing *T* by *S* yielded the ratio between tumor tissues and background level. Semiquantitative data can be obtained from the fluorescence images by drawing ROI on the area to be quantified. The results are expressed as a number of relative light units per pixel (RLU/pix).

At the end of *in vivo* imaging experiment, the animals were killed (Dolethal, 1 μL g^{-1} intracardiac), on day 15 for HCT 116 model and on days 2 and 3 for glioblastoma multiforme and A549. The blood, main organs such as heart, lungs, brain, skin, thigh muscle, adrenals, bladder, intestine, spleen, pancreas, fat, stomach, womb, ovaries, liver and tumor were removed and analyzed using the system described previously.

Statistics. GraphPad Prism Software (GraphPad Software) was used to perform statistical analyses and graphical presentation. Experiments were reproduced at least two times. Data were expressed as mean ± SDs, *n*. Statistical analyses in Table 1 were obtained using Student's *t*-test.

RESULTS

Impact of nanoparticles size on cell viability and internalization

In Fig. 1a, three different Pp IX silica nanoparticle sizes (10, 25 and 60 nm) were evaluated by TEM. Other chemical criteria were also confirmed by TEM such as monodispersity, spherical shape and reproducibility of batch. Next, the different sizes were tested in *in vitro* on HCT 116 cell line (Fig. 1b), after 3 h incubation with nanoparticles, illuminated immediately after for 20 min with a lamp. WST-1 cell viability tests demonstrated equivalent results for all sizes with EC$_{50}$ (50% effective concentration) at 0.44 μM (±0.05). To better understand the impact of nanoparticle size on HCT 116 cell internalization, the amount of internalized nanoparticles after 0.5, 1 and 3 h incubation at fixed 5 μM concentration were quantified (Fig. 1c). No significant difference of internalization kinetic and total amount of nanoparticle uptake (150, 200 and 400 fmol per 1000 cells after 0.5, 1 and 3 h of incubation) was measured.

Hence, all *in vitro* and *in vivo* tests were performed with Pp IX silica nanoparticles centered at 25 nm.

Uptake and clearance of Pp IX silica nanoparticles

Internalized photosensitizers are the source of photodamage, as for nanoparticulated products. Furthermore, the subcellular

Table 1. EC$_{50}$ (μM) in different cell lines: HCT 116, HT-29, A431, LLBC37, MCF7 and MDA-MB-231.

Cell line	Cell viability Pp IX silica nanoparticles (†EC$_{50}$; μM)	Cell viability free Pp IX (EC$_{50}$; μM)
HCT 116	0.44 ± 0.05	6.03 ± 0.43*
HT-29	0.72 ± 0.21	9.60 ± 0.96*
A431	1.01 ± 0.07	32.68 ± 1.77*
LLBC37	0.40 ± 0.01	3.44 ± 0.36*
MCF7	0.99 ± 0.14	15.59 ± 1.15*
MDA-MB-231	1.13 ± 0.15	8.19 ± 0.76*

*Represents $P < 0.0001$ as obtained using Student's *t*-test, where the statistical significance between Pp IX silica nanoparticles and free Pp IX cell viability was shown.†EC$_{50}$, 50% effective concentration was calculated using sigmoidal-fit function of GraphPad Prism software. Experiments were carried out in duplicate and data are mean of at least three independent experiments. Pp IX = Protoporphyrin IX.

localization seems to be a key parameter to determine efficient pathway of cell death. As shown in Fig. 2a, HCT 116 cells treatment with Pp IX silica nanoparticles during 3 h at 4°C and illuminated immediately after, yielded cell death with an $EC_{50} = 0.4$ μM, which is equivalent to the value obtained when the cells were incubated at 37°C. However, total amount of nanoparticles uptake was lower at 4°C than at 37°C (data not shown). These results suggested balance between passive and active internalization. Indeed, Pp IX silica nanoparticles were efficient at temperature with extreme metabolic downregulation, which may involve higher proportion of passive internalization. In addition, accumulation of Pp IX silica nanoparticles and free Pp IX was observed within the cytoplasm of cells. No signal was observed in the nucleus (data not shown).

The question of nanoparticles clearance was also addressed (Fig. 2b). Cells were treated 3 h with various concentrations of Pp IX silica nanoparticles, or free Pp IX (Fig. 2c), then medium was removed and fresh complete medium was added. At 2 and 5 h after the end of incubation, HCT 116 cell line was illuminated. Results showed loss of efficiency using WST-1 assay. At 2 h, and for the maximal concentration of Pp IX silica nanoparticles or free Pp IX, the most marked efficiency decrease of nanoparticles was observed with cell survival of 40%. Furthermore, differences of curves appearances were observed between Pp IX silica nanoparticles (stage) and free Pp IX (dose effect). Meanwhile, free Pp IX incubated cells did behavior differently with 0% of cell survival. Loss of efficiency was found for both systems at 5 h illumination time point. When light activation was performed 24 h after the end of incubation, no residual activity of both Pp IX silica nanoparticles and free Pp IX was observed. Different hypotheses may be envisaged, the cell clearance of Pp IX silica nanoparticles or a degradation of these particles within the cytoplasm,

which might neutralize efficiency of singlet $^1O_2$, critical for successful PDT. To examine this question, medium was changed after 3 h incubation and retrieved 24 h later. It was filtered with Amicon membrane (30 000 Da) to concentrate it. Medium UV absorbance demonstrated abundant presence of Pp IX silica nanoparticles, which is alike of absorbance of internalized Pp IX silica nanoparticles quantified in cell pellets (data not shown). Cell clearance was proved to determine the lack of efficiency in HCT 116 cell line.

Pp IX nanoparticle effects on cell survival

In our study, 3 h incubation with Pp IX silica nanoparticles had the maximal effect on decreasing tumor cell survival (WST-1) of HCT 116 cancer cell line. Shorter incubations achieved less efficient cell death. Further, any performance improvement was detected with prolonged times, 5 and 12 h (data not shown). Then, we tested the time of illumination (2, 5, 10 and 20 min with lamp, maximal intensity ≈50 μW cm^{-2}) on HCT 116 for Pp IX silica nanoparticles and for free Pp IX. Most efficient illumination time was 20 min; its prolongation did not show any advantage in terms of cell death (data not shown).

Thus, 3 h incubation and 20 min of illumination were used for cell viability assessment with Pp IX silica nanoparticles or free Pp IX in HT-29, A431, LLBC37, MCF7 and MDA-MB-231 tumor cell lines (Table 1). In all tumor types, Pp IX silica nanoparticles were more efficient (more than one log of difference; $P < 0.0001$) than free Pp IX.

In addition, A431, MCF7 and MDA-MB-231 cell lines showed EC_{50} similar values. HCT 116, an adherent and LLBC37 a suspension cell lines shared also very similar EC_{50} values despite their different biological characteristics in terms of adherence. Regarding HT-29, it seems to have a different sensitivity with the observed highest standard deviation.
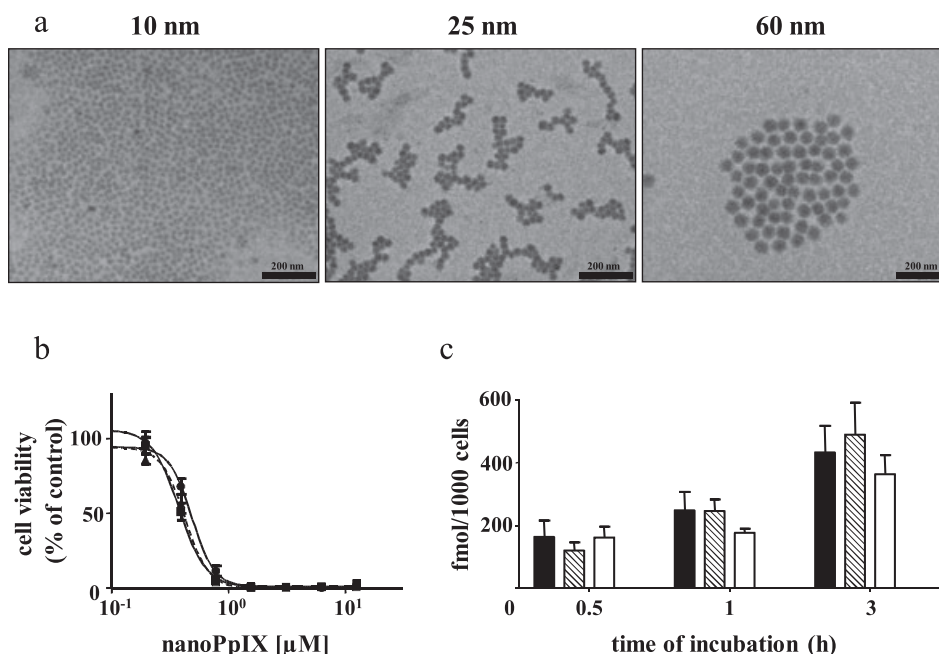

Figure 1. Impact of Pp IX silica nanoparticles size on viability and internalization on HCT 116. (a) Pp IX silica nanoparticles sizes evaluated by TEM. Scale bar, 200 nm. (b) Cell viability of different Pp IX silica nanoparticles sizes after activation: ●, 10 nm; ■, 25 nm; and ▲, 60 nm. (c) Quantitative analysis of different Pp IX nanoparticles size on cell internalization: ■, 10 nm; ▨, 25 nm; and □ 60 nm.
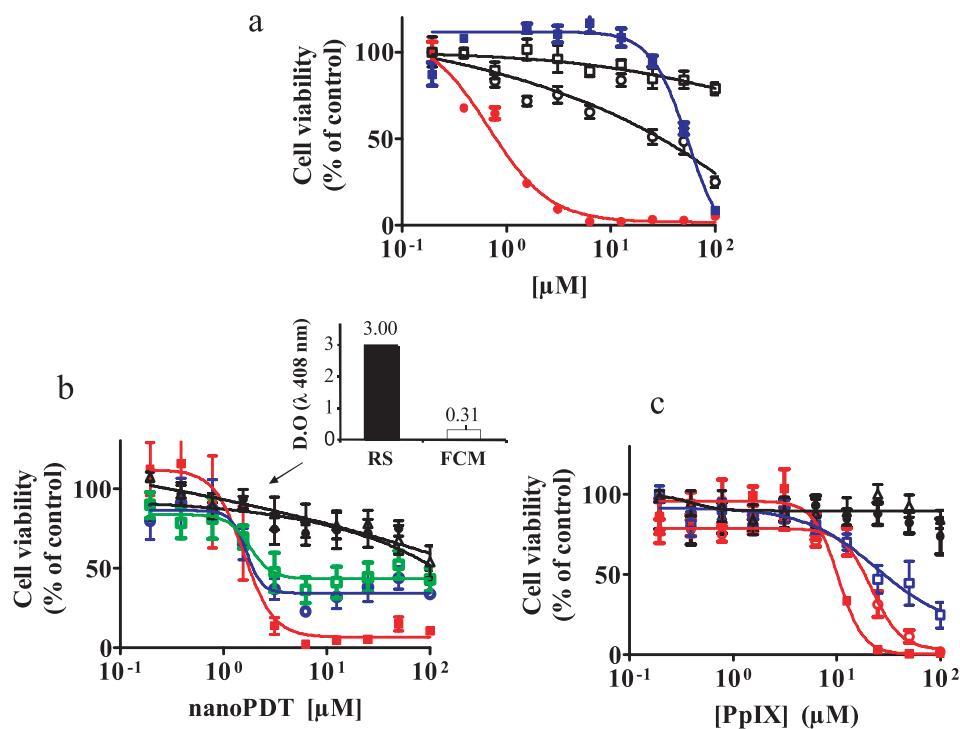
Figure 2. Uptake and clearance of Pp IX silica nanoparticles and free Pp IX on HCT 116. (a) Cell viability of Pp IX silica nanoparticles with (●) or without (○) activation; free Pp IX with (■) or without (□) activation after 3 h of incubation at 4°C. (b) Cell viability of Pp IX silica nanoparticles at different time of light activation after the end of incubation ■, 0 min (●; without activation); ○, 2 h; □, 5 h; △, 24 h. D.O absorbance values at 408 nm of reconcentrated solution (RS) and fresh culture medium (FCM) for the time 24 h. (c) Cell viability of free Pp IX at different time of light activation after the end of incubation ■, 0 min; ○, 2 h; □, 5 h; ▲, 24 h (●,without activation).

ROS generation and quantification of cell internalization

Upon laser light absorption, the Pp IX molecule is excited. This excited molecule interacts with the biological environment to produce ROS, including singlet oxygen ($^1O_2$), superoxide anion (O_2^-) and hydroxyl radical ($OH^\bullet$) which are responsible for cell damages (10,11). Two kinds of reaction can occur. In a Type 1 reaction, the excited molecule can react directly with the substrate, such as the cell membrane or a molecule, and transfer a proton or an electron to form a radical anion or cation. These radicals may further react with oxygen to produce ROS. Alternatively in a Type 2 reaction, the excited molecule can transfer its energy directly to molecular oxygen to form excited state singlet oxygen. Both Type 1 and Type 2 reactions can occur simultaneously, and the ratio between these processes depends on the type of photosensitizer used, as well as the concentrations of substrate and oxygen. ROS detection was performed using APF kit. Figure 3 shows the correlation between cell amount of ROS and free Pp IX or Pp IX silica nanoparticle concentrations in HCT 116 and HT-29 cell lines (Fig. 3a and b). For Pp IX silica nanoparticles, strong fluorescence signal of ROS liberation is correlated with 100% of cell death in both colon cancer cell lines. For Pp IX, results were similar and correlated with EC_{50}; however, global fluorescence intensity signals were weaker for each tested product concentration. This variation may be the basis of cell death efficiency, which is well superior for Pp IX encapsulated within the silica shells.

As the efficiency of PDT can be attributed to the production ROS (11), Pp IX nanoparticles silica matrixes present a relevant range of porosity to allow the entrapped photosensitizer to interact with molecular oxygen, leading to the formation of singlet oxygen, which can then diffuse out of the porous matrix to produce a cytotoxic effect in tumor cells.

In addition, under the same experimental conditions, HT-29 fluorescence signal is weaker at any tested concentration of Pp IX silica nanoparticles when HCT 116 and HT-29 cell lines are compared, which may ultimately modify the PDT efficiency in the first cell line.

Consequently, the amount of internalized nanoparticles was investigated on cell lines with quantitative assays to compare after 0.5, 1 and 3 h incubations at fixed 5 μM concentration (Fig. 3c). Internalization kinetic was different between HT-29 and HCT 116 cell lines. After 3 h of incubation, 600 fmol per 1000 cells and 200 fmol per 1000 cells of nanoparticles were observed in HCT 116 and HT-29 cells, respectively. Correlation of internalized nanoparticles amount to detection of ROS suggests that HT-29 cell type internalized less Pp IX silica nanoparticles, which was followed by diminution of ROS generation. The short migration distance of singlet oxygen, less than 0.02 μm and its extremely short lifetime, 52 μs (12) determine a strong relationship between the sites of subcellular localization of the Pp IX and photodamage to nearby organelles involved in cell death. We have shown the intracellular localization of ROS in HCT 116 cells after 3 h of incubation with Pp IX silica nanoparticles at 1 μM. Moreover, ROS were colocalized with the nanoparticles within the cytoplasm as visualized with a fluorescent microscope (Fig. 3d).
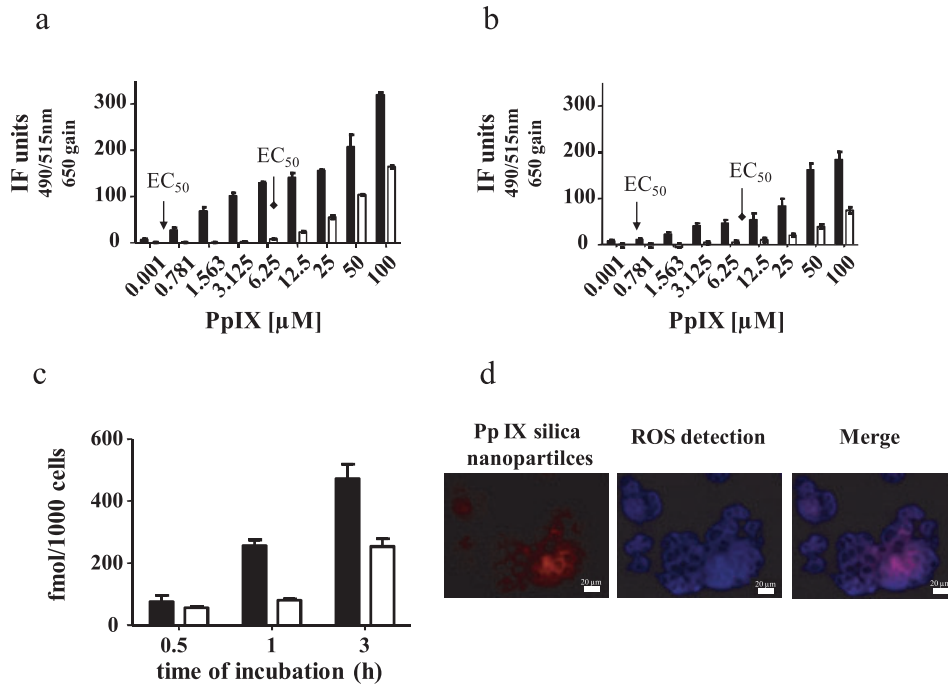
a

b

c

d

Figure 3. ROS generation of Pp IX silica nanoparticles and free Pp IX and quantification of cell internalization on HCT 116 and HT-29. (a) Correlation between ■ Pp IX silica nanoparticles and □ free Pp IX range of concentrations and ROS generation on HCT 116. (b) Correlation between ■ Pp IX silica nanoparticles and □ free Pp IX range of concentrations and ROS generation on HT-29. (c) Quantitative assays to compare the amount of internalized Pp IX silica nanoparticles after 0.5, 1 and 3 h of incubation on ■ HCT 116 and on □ HT-29. (d) Cytoplasmic localization of Pp IX silica nanoparticles and of ROS liberation on HCT 116. Colocalization between nanoparticles and ROS liberation (merge). Fluorescence images, scale bar represents 20 μm; 40× lens.
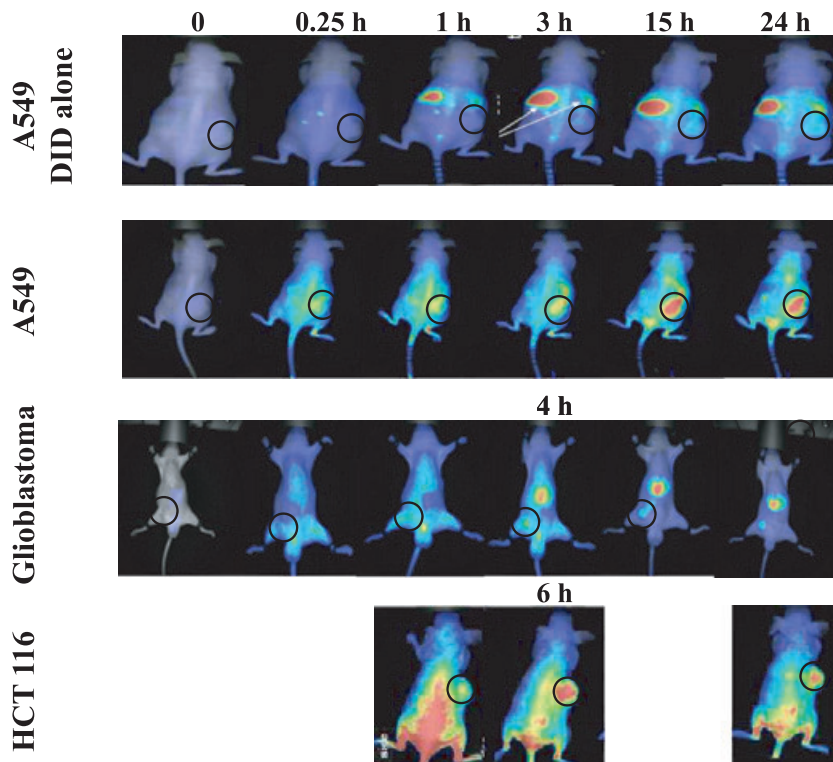

Figure 4. Biodistribution *in vivo* of DID alone on A549 and with Pp IX silica nanoparticles on A549 cell line, glioblastoma multiforme model and HCT 116 cell line. Comparative fluorescence at 0, 0.25, 1, 15 and 24 h after Pp IX silica nanoparticles injection and at 3 and 4 h for A549 and glioblastoma multiforme, respectively. Pp IX silica nanoparticles were visualized after 1, 6 and 24 h of injection in HCT 116 model.

Biodistribution of Pp IX silica nanoparticles loaded with DID tracer in tumor-bearing animals: whole body optical imaging

Nude mice-bearing HCT 116, A549 tumors and glioblastoma multiforme tumors were imaged before intravenous injection (baseline) of Pp IX silica nanoparticles loaded with DID tracer. As similar qualitative distribution was observed in the three mouse models for Pp IX silica nanoparticles loaded with DID tracer, the biodistribution of the free DID tracer was explored in the A549 model to establish prospective comparator. Images were obtained at different time points after nanoparticles tail vein injection (0, 0.25, 1, 3 ± 3 depending on the model, 15 and 24 h).

As shown in Fig. 4, high tumor uptake of Pp IX silica nanoparticles loaded with DID tracer was observed in the three models. The DID tracer did not accumulate at the tumor site and was mainly present in liver, spleen and lymph nodes, underlining the differential distribution of dye entrapped in silica nanoparticles. The semiquantitative analysis showed that the tumor models reached maximal accumulation of nanoparticles at different time points: 2 h for glioblastoma multiforme, 16 h for A549 and 20 h for HCT 116 models, respectively. Regarding the glioblastoma multiforme model, the nanoparticles uptake took place rapidly after injection and was maximal at 2 h, while a marked decrease was observed

immediately later. Concerning the A549 tumor, the accumulation within the tumor structure was achieved slowly without image changes until 24 h when the Pp IX silica nanoparticles loaded with DID tracer signal remained elevated. HCT 116 model behaved similarly. In normal skin, over time kinetic curves of Pp IX silica nanoparticles loaded with DID tracer were similar to kinetic curves observed for tumors, but the accumulation ratio was markedly lower in skin when compared with tumor (at 24 h, tumor: 12 080, skin: 8933 RLU/-pix). Decrease of fluorescence in skin was more rapidly achieved. Consequently, the tumor/skin ratio = 3 significantly increased up to 24 h after injection. Tumor/skin ratio was 1.6 between 5 and 16 h.

At each time point, the nanoparticles showed a better tumor accumulation than the control DID alone, which demonstrates more selectivity of Pp IX silica nanoparticles loaded with DID tracer for tumor tissues. Finally, the tumor contrast (T/S ratio) was markedly enhanced in glioblastoma multiforme tumor model: the T/S ratio reached the value of 2.96 at 24 h post injection. This was significantly higher than T/S ratios observed for HCT 116 and A549 tumor models (1.7 and 1.6, respectively). With respect to healthy tissues, nanoparticles exhibited prominent accumulation in the liver, higher than that within the tumor mass. Furthermore, they were present in spleen, lymph nodes, ovaries, lungs and adrenal glands. Later,
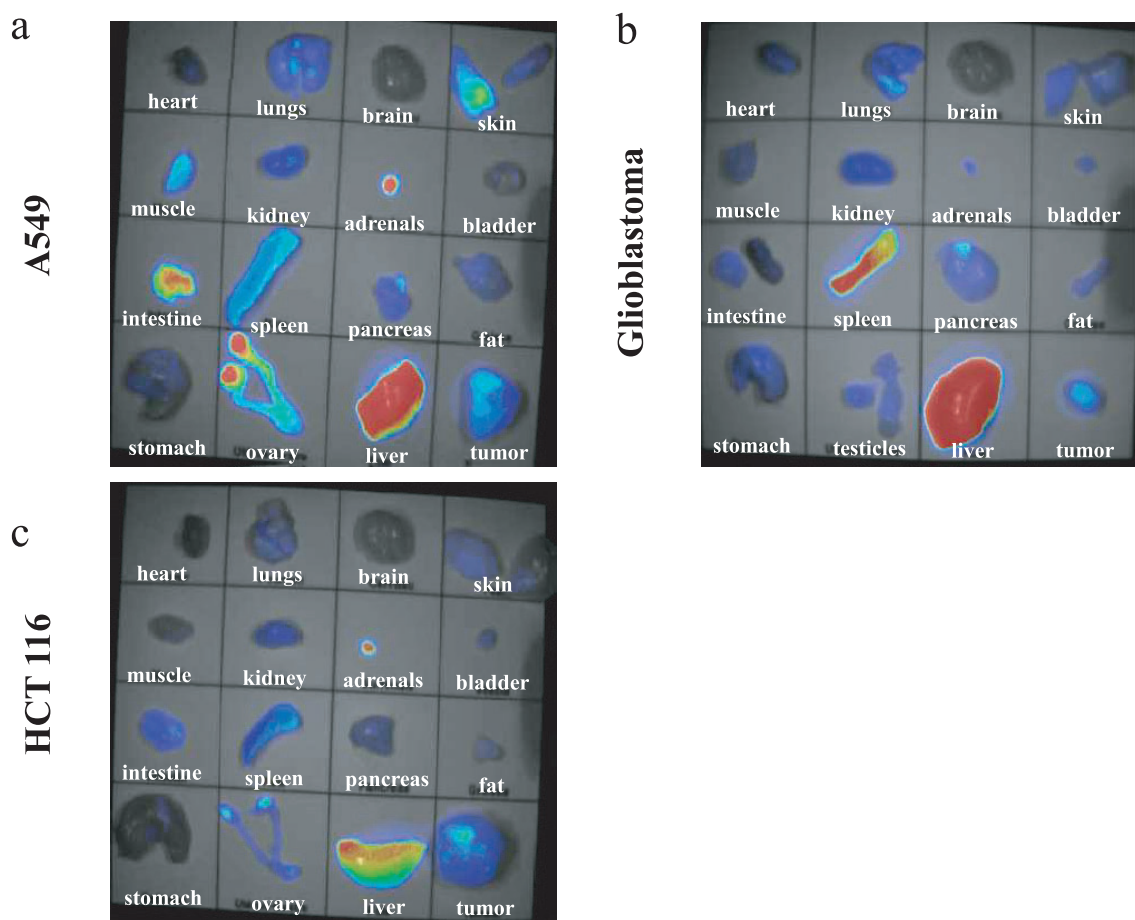

Figure 5. Fluorescence of mouse isolated organs: heart, lungs, brain, skin, muscle, kidney, adrenals, bladder, intestine, spleen, pancreas, fat, stomach, womb–ovary/testicles, liver and tumor. (a) A549: dissection after 24 h after intravenous injection. (b) Glioblastoma multiforme: dissection after 24 h after intravenous injection. (c) HCT 116: dissection after 16 days after intravenous injection.

in an attempt to better observe the nanoparticles' relative accumulation among different body tissues, mice were killed and organs were analyzed under optical imaging system. Figure 5 confirmed that the tumor and the liver were the two tissue types showing the strongest nanoparticle-related fluorescence, whereas the female genital parts, the spleen and the adrenal glands exhibited substantial fluorescence. In most tissue types, the fluorescence intensities decreased over time. Liver was the exception, notably the intensity remained remarkably constant over the time period investigated. No urine elimination was observed throughout the imaging observation period.

DISCUSSION

Photodynamic therapy in the elderly and heavily pretreated cancer patient populations may represent a promising therapeutical option in the management of malignant diseases provided that different approaches bring real improvement for its clinical application.

In the past decade, the field of drug delivery was revolutionized by the advent of nanotechnology; biocompatible nanoparticles were developed as inert systemic carriers for therapeutic compounds to target cells and tissues (13,14).

Most photosensitizing drugs such as Pp IX are hydrophobic, *i.e.* poorly water soluble, and therefore, preparation of pharmaceutical formulations for parenteral administration is highly hampered (15–18). To overcome this difficulty, different strategies have evolved to enable a stable dispersion of these drugs into aqueous systems, often by means of a delivery vehicle.

Prasad and colleagues (19) encapsulated hexyloxy ethyl 2 devinyl pyropheophorbide-a, a photosensitizer that is currently undergoing clinical trials for esophageal cancer in silica-based nanoparticles. Also, entrapment of Pp IX in silica nanoparticles was achieved for PDT (12,20).

To develop stable and efficient systemic carriers for hydrophobic anticancer compounds, our laboratory has developed silica nanoparticles containing Pp IX. Nonbiodegradable nanoparticles offer several advantages such as the design of complex platforms with association of different agents within the same nanostructure. Here, a one pot synthesis of new hybrid nanocarrier was performed. No modification of the photosensitizer molecule was attempted to covalently link the photosensitizer to the nanoparticles. Instead, a physical encapsulation was performed with the will to simplify as much as possible both the product synthesis route and its final composition. Previous preclinical studies have demonstrated the essential nontoxicity of this Pp IX silica nanoparticle formulation in *in vitro* and interestingly, a very good tolerance in *in vivo* models (unpublished data), and the potential of these nanoparticles as carriers for hydrophobic drugs. Furthermore, in the literature, one *in vivo* mouse study has showed that silica nanoparticles are well tolerated (21).

Regarding the size, it seems to be an important parameter which influences the way metallic nanoparticles enter cells and how it impacts on cell functions (22). Published data highlighted 10–100 nm size range as the best for cell uptake. Citric acid gold nanoparticles demonstrated the best internalization at 50 nm (23). As far as we know, few comparative studies of different silica-based nanoparticle sizes have been performed

to determine the size role on cell uptake and pathways. Pertinent evaluation of their physical parameters should take into account the multiple chemistries involved in the silica nanoparticle productions. Jin *et al.* used a water-in-oil microemulsion synthesis with systematically varying the organic solvent to control the size of silica nanoparticles within the nanometer range (20 nm up to 100 nm). The effect of nanoparticle size on their ability to penetrate human cancer cell line (A549) cellular membranes was studied using two sizes of nanoparticles. The small nanoparticles (23 nm) clearly were shown to penetrate the cells faster than the large nanoparticles (85 nm) (24). Lu *et al.* (25) examined the size effect of fluorescein isothiocyanate–mesoporous silica nanoparticles, with uniform size ranging from 30 to 280 nm, on HeLa cell uptake. The authors found that cell uptake was clearly nanoparticle size-dependent in the order $50 > 30 > 110 > 280 > 170$ nm. Interestingly, the optimum size of 50 nm for cell uptake was found to be similar to the cell uptake of gold nanoparticles recently reported (23).

In our study, Pp IX silica nanoparticles of 10, 25 and 60 nm showed behavior in the same way concerning cell uptake and cell viability. Further investigation have shown that Pp IX silica nanoparticles were found to be efficient at temperature with extreme metabolic downregulation which suggest a high proportion of passive internalization with accumulation within the cytoplasm of cells. This type of mechanism could explain the absence of effect of our nanoparticles size on cell uptake.

For 60 nm, total amount of Pp IX per nanoparticle can be increased and thus allows optimization of bioavailability in *in vivo* models.

All type of photosensitizers can be internalized in tumor cell lines but kinetic, localization and properties change in function of coating, charge, size and shape. Pp IX silica nanoparticle uptake was dependent upon cell type, as evident by the greater uptake into HCT 116 cells. Of note, HT-29 cells have larger cell volume (around two times for the cytoplasm) than that of HCT 116 cells and thus, they may passively internalize more nanoparticles. Further, the larger HT-29 cells tended to have the lowest uptake. Thus, differential cell capture could be explained by a significant difference of endocytosis mechanism or by a difference between uptake and clearance ratios between the two cell lines.

Most photosensitizer molecules such as Pp IX are hydrophobic and can aggregate easily in aqueous media, which can affect their photophysical, chemical and biological properties (26). In our studies, kinetic of internalization of Pp IX silica nanoparticles was variable following the cell type, slower and less nanoparticles internalization was seen in HT-29 cell line. Furthermore, maximum difference was observed after 3 h of incubation (data not shown). The experiments supposed a saturation threshold in their intracellular accumulation at this time point without any evidence of toxicity. Similar features in G361 melanoma cells, using a second generation of sensitizers, phthalocyanine ClAlPcS$_2$ were found (27). This state of saturation might be due to depletion of endocytotic mechanisms, saturation of the storage capacity of the cells or uptake/clearance balance.

For the first time, clearance of silica nanoparticles on tumor cells is reported. In our study, 2 h after new medium addition, cell death efficiency was decreased, likely related to nanoparticles release. Indeed, 24 h after medium change most of the

nanoparticles were collected in the supernatant. Clearance seems to begin early, before 2 h. For citric acid gold nanoparticles (14–74 nm range), clearance was demonstrated to begin within 30 min, and to be higher for smaller nanoparticles (28).

All photosensitizers, which are now approved for clinical use were found to be localized in the cytoplasmic with different specific suborganella area (29). The cells treated with Pp IX silica nanoparticles showed fluorescence diffusively distributed throughout the cytoplasm, with a nonfluorescent nuclear area in six different cells lines. As suborganella localization may be crucial for PDT efficiency, further studies are needed to elucidate this feature using selective fluorescent probes.

Reactive oxygen species had a short lifetime and migration distance during this period (12). Therefore, the initial extent of the damage is limited to the site of concentration of the nanoparticles (29).

Our results demonstrated that ROS generation is significantly improved in the presence of Pp IX silica nanoparticles in both HCT 116 and HT-29 cells lines: higher concentrations yielded more marked difference. Higher ROS amounts cause larger cell photodamage and consequently better phototoxic effect.

Biodistribution is an important parameter of the *in vivo* behavior and determine pathways of possible interactions of nanoparticles and cells in term of efficacy and safety. Few works focused on pharmacokinetics of silica nanoparticles have been reported and no data from tumor-bearing animal models is currently known. Fluorescent silica nanoparticles tuned to hydrodynamic diameters of 3.3 and 6 nm with neutral coating prevented opsonization and showed high renal excretion at 45 min postinjection in male nude mice. It is noteworthy that 5.5 nm can be considered as the threshold for glomerular filtration (30). Fluorescence quantification in postmortem evaluation revealed minimal retention in major organs, less than 5% for 3 nm and 20% for 6 nm nanoparticles at 6 h postinjection (31). Silica nanoparticles tuned at 45–47 nm, with 3 coatings (negative/positive/neutral) were also evaluated for biodistribution and excretion (32). Male nude mice and female Sprague–Dawley rats were assessed for urinary excretion. Results showed that the three types were cleared from the bloodstream and were present in organs. *In vivo* imaging revealed accumulation in liver, bladder, kidney and spleen. Twenty-four hours postinjection, some fluorescence was present in the mentioned organs confirming the partial dose renal excretion of the nanoparticles.

In this work, *in vivo* studies were performed in tumor-bearing animals which permitted first observations on tumor/skin ratio accumulation of the product. Similar distribution in main organs was observed in the three mouse models for Pp IX silica nanoparticles loaded with DID tracer. The accumulation in tumor was, at least partially, a passive process and due to the known tumor vessel characteristics such as enhanced permeability and retention effect. However, kinetics demonstrated by semiquantitative analysis showed that tumor models behaved differently according to the maximal accumulation time point: 2 h for glioblastoma multiforme, 16 h for A549 and 20 h for HCT 116 models, respectively. As observed in *in vitro* tests, tumor cell type is likely a major determinant also. Furthermore, anatomical site of the xenograft may play a minor role. Xenograft structure could more influence this differential time

accumulation dynamic; glioblastoma multiforme was inserted as a fragment, stroma natural cells were present.

In vivo, favorable tumor-to-normal tissue ratios have been observed for many photosensitizers. Pharmacokinetic specificities and pathology and tumor functions seem to influence these ratios (33). Healthy skin and tumor structure showed similar time kinetic curves of Pp IX silica nanoparticles loaded with DID. Nevertheless, the accumulation ratio was markedly lower in skin when compared with tumor and skin fluorescence diminution was more rapidly achieved. Tumor/skin ratio demonstrated significant elevation at the latest evaluated time point (16 h). As skin disorders represent a major caveat of PDT, a clear understanding and knowledge of Pp IX silica nanoparticles kinetics in these systems is to be explored in specific studies. Postmortem isolated organs completed specific organ distribution information. Of note, liver fluorescence intensity remained remarkably constant over the time period investigated and no urine excretion was found.

The present findings, reinforced by the observation that silica nanoparticles are well tolerated in other cell systems strengthen the hypothesis that the Pp IX silica nanoparticles may be involved in new alternative local applications of PDT, which would allow dose administration of photosensitizers and establishment of the optimal illumination schedule following specific cancer types. Moreover, they suggest the possibility of different profile of photosensitizer adverse events and open the way to achieve better control of systemic photosensitization.

REFERENCES

1. Zuluaga, M. F. and N. Lange (2008) Combination of photodynamic therapy with anti-cancer agents. *Curr. Med. Chem.* **15**, 1655–1673.
2. Oleinick, N. L., R. L. Morris and I. Belichenko (2002) The role of apoptosis in response to photodynamic therapy: What, where, why, and how. *Photochem. Photobiol. Sci.* **1**, 1–21.
3. Fritsch, C., K. Lang, W. Neuse, T. Ruzicka and P. Lehmann (1998) Photodynamic diagnosis and therapy in dermatology. *Skin Pharmacol. Appl. Skin Physiol.* **11**, 358–373.
4. Mimura, S., H. Narahara, H. Uehara, T. Otani and S. Okuda (1996) Photodynamic therapy for gastric cancer. *Gan To Kagaku Ryoho.* **23**, 41–46.
5. Kato, H., N. Kawate, K. Kinoshita, H. Yamamoto, K. Furukawa and Y. Hayata (1989) Photodynamic therapy of early-stage lung cancer. *Ciba Found. Symp.* **146**, 183–197.
6. Muroya, T., Y. Suehiro, K. Umayahara, T. Akiya, H. Iwabuchi, H. Sakunaga, M. Sakamoto, T. Sugishita and Y. Tenjin (1996) Photodynamic therapy (PDT) for early cervical cancer. *Gan To Kagaku Ryoho.* **23**, 47–56.
7. Taillandier, L., L. Antunes and K. S. Angioi-Duprez (2003) Models for neuro-oncological preclinical studies: Solid orthotopic and heterotopic grafts of human gliomas into nude mice. *J. Neurosci. Methods* **125**, 147–157.
8. Garanger, E., D. Boturyn, Z. Jin, P. Dumy, M. C. Favrot and J. L. Coll (2005) New multifunctional molecular conjugate vector for targeting, imaging, and therapy of tumors. *Mol. Ther.* **12**, 1168–1175.

9. Jin, Z. H., V. Josserand, J. Razkin, E. Garanger, D. Boturyn, M. C. Favrot, P. Dumy and J. L. Coll (2006) Noninvasive optical imaging of ovarian metastases using Cy5-labeled RAFT-c(-RGDfK-)4. *Mol. Imaging* **5**, 188–197.

10. Robertson, C. A., D. H. Evans and H. Abrahamse (2009) Photodynamic therapy (PDT): A short review on cellular mechanisms and cancer research applications for PDT. *J. Photochem. Photobiol. B* **96**, 1–8.

11. Josefsen, L. B. and R. W. Boyle (2008) Photodynamic therapy and the development of metal-based photosensitisers. *Met. Based Drugs* **2008**, 276109–276133.

12. Rossi, L. M., P. R. Silva, L. L. Vono, A. U. Fernandes, D. B. Tada and M. S. Baptista (2008) Protoporphyrin IX nanoparticle carrier: Preparation, optical properties, and singlet oxygen generation. *Langmuir* **24**, 12534–12538.

13. Konan, Y., R. Gurny and E. Allémann (2002) State of the art in the delivery of photosensitizers for photodynamic therapy. *J. Photochem. Photobiol. B* **66**, 89–106.

14. Hasan, T., A. C. E Moor and B. Ortel (2000). *Cancer Medicine*, 5th edn. B.C. Decker, Inc., Hamilton, ON.

15. Dougerthy, T. J. (1987) Photosensitizers: Therapy and detection of malignant tumors. *Photochem. Photobiol.* **45**, 879–889.

16. Taillefer, J., M. C. Jones, N. Brasseur, J. E. van Lier and J. C. Leroux (2000) Preparation and characterization of pH-responsive polymeric micelles for the delivery of photosensitizing anticancer drugs. *J. Pharm. Sci.* **89**, 52–62.

17. Van-Vlerken, L. E. and M. M. Amiji (2006) Multi-functional polymeric nanoparticles for tumour-targeted drug delivery. *Expert Opin. Drug Deliv.* **3**, 205–216.

18. Torchilin, V. P. (2007) Nanocarriers. *Pharm. Res.* **24**, 2333–2334.

19. Roy, I., T. Y. Ohulchanskyy, H. E. Pudavar, E. J. Bergey, A. R. Oseroff, J. Morgan, T. J. Dougherty and P. N. Prasad (2003) Ceramic-based nanoparticles entrapping water-insoluble photosensitizing anticancer drugs: A novel drug-carrier system for photodynamic therapy. *J. Am. Chem. Soc.* **125**, 7860–7865.

20. Tu, H. L., Y. S. Lin, H. Y. Lin, Y. Hung, L. W. Lo, Y. F. Chen and C. Y. Mou (2009) *In vitro* studies of functionalized mesoporous silica nanoparticles for photodynamic therapy. *Adv. Mater.* **21**, 172–177.

21. Xue, Z. G., S. H. Zhu, Q. Pan, D. S. Liang, Y. M. Li, X. H. Liu, K. Xia and J. H. Xia (2006) Biotoxicology and biodynamics of silica nanoparticle. *J. Cent. South Univ. (Med. Sci)* **31**, 6–8.

22. Ferrari, M. (2008) Nanogeometry: Beyond drug delivery. *Nat. Nanotechnol.* **3**, 131–132.

23. Chithrani, B. D., A. A. Ghazani and W. C. Chan (2006) Determining the size and shape dependence of gold nanoparticle uptake into mammalian cells. *Nano. Lett.* **6**, 662–668.

24. Jin, Y., S. Lohstreter, D. T. Pierce, J. Parisien, M. Wu, C. Hall and J. X. Zhao (2008) Silica nanoparticles with continuously tunable sizes: Synthesis and size effects on cellular contrast imaging. *Chem. Mater.* **20**, 4411–4419.

25. Lu, F., S. H. Wu, Y. Hung and C. Y. Mou (2009) Size effect on cell uptake in well-suspended, uniform mesoporous silica nanoparticles. *Small* **5**, 1408–1413.

26. Bechet, D., P. Couleaud, C. Frochot, M. L. Viriot, F. Guillemin and M. Barberi-Heyob (2008) Nanoparticles as vehicles for delivery of photodynamic therapy agents. *Trends Biotechnol.* **26**, 612–621.

27. Kolarova, H., P. Nevrelova, R. Bajgar, D. Jirova, K. Kejlova and M. Strnad (2007) *In vitro* photodynamic therapy on melanoma cell lines with phthalocyanine. *Toxicol. In Vitro* **21**, 249–253.

28. Chithrani, B. D. and W. C. Chan (2007) Elucidating the mechanism of cellular uptake and removal of protein-coated gold nanoparticles of different sizes and shapes. *Nano. Lett.* **7**, 1542–1550.

29. Chatterjee, D. K., L. S. Fong and Y. Zhang (2008) Nanoparticles in photodynamic therapy: An emerging paradigm. *Adv. Drug. Deliv. Rev.* **60**, 1627–1637.

30. Li, S. D. and L. Huang (2008) Pharmacokinetics and biodistribution of nanoparticles. *Mol. Pharm.* **5**, 496–504.

31. Burns, A. A., J. Vider, H. Ow, E. Herz, O. Penate-Medina, M. Baumgart, S. M. Larson, U. Wiesner and M. Bradbury (2009) Fluorescent silica nanoparticles with efficient urinary excretion for nanomedicine. *Nano. Lett.* **9**, 442–448.

32. He, X., H. Nie, K. Wang, W. Tan, X. Wu and P. Zhang (2008) *In vivo* study of biodistribution and urinary excretion of surface-modified silica nanoparticles. *Anal. Chem.* **80**, 9597–9603.

33. Ben-Dror, S., I. Bronshtein, A. Wiehe, B. Roder, M. O. Senge and B. Ehrenberg (2006) On the correlation between hydrophobicity, liposome binding and cellular uptake of porphyrin sensitizers. *Photochem. Photobiol.* **82**, 695–701.